Laminar-Turbulent Transition Upstream of the Entropy-Layer Swallowing Location in Hypersonic Boundary Layers

Pedro Paredes,*
National Institute of Aerospace, Hampton, VA 23666, USA

Meelan M. Choudhari,† Fei Li,‡
NASA Langley Research Center, Hampton, VA 23681, USA

Numerical and experimental studies have demonstrated that modal growth of planar Mack modes is responsible for laminar-turbulent transition on sharp cones at hypersonic speeds. However, the physical mechanisms that lead to transition onset upstream of the entropy-layer swallowing location over sufficiently blunt geometries are not well understood as yet. Modal amplification is too weak or nonexistent to initiate transition at moderate-to-large bluntness values. Nonmodal analysis shows that, with increasing nose bluntness, both planar and oblique traveling disturbances that peak within the entropy layer experience appreciable energy amplification. However, because of the relatively weak signature of the nonmodal traveling disturbances within the boundary-layer region, the route to transition onset subsequent to the nonmodal growth remains unclear. Thus, nonlinear parabolized stability equations (NPSE) and direct numerical simulations (DNS) have been used to investigate the potential transition mechanisms over a 7-degree blunt cone that was tested in the AFRL Mach-6 high-Reynolds-number facility. Computations are performed to separately follow the nonlinear development of two classes of inflow disturbances, namely, a pair of oblique traveling waves with equal but opposite angles with respect to the mean flow direction and a planar traveling wave. Results in both cases show an excellent agreement between the NPSE and DNS predictions, establishing that the NPSE is an accurate and efficient technique for predicting the nonlinear development for these particular nonmodal traveling disturbances. Computations reveal that the oblique mode interactions lead to the generation of stationary streaks inside the boundary layer that, in turn, facilitate the growth of a subharmonic sinuous disturbance. For relatively modest amplitudes of the inflow disturbance, the oblique-mode breakdown can lead to transition at the measured location of transition onset during the experiment. On the other hand, the nonlinear development of a planar traveling wave leads to the formation of inclined structures just above the boundary-layer edge and these structures are strongly reminiscent of the transitional events observed during blunt cone experiments by using schlieren flow visualizations.

Nomenclature

E	=	total energy norm
F	=	disturbance frequency [s^{-1}]
h_t	=	total enthalpy [$kg \cdot m^2 \cdot s^{-2}$]
h_ξ	=	streamwise metric factor
h_ζ	=	azimuthal metric factor [m]
L	=	reference length [m]
m	=	azimuthal wavenumber [rad^{-1}]
M	=	Mach number
N	=	Logarithmic amplification factor
$\hat{\mathbf{q}}$	=	vector of amplitude variables
$\check{\mathbf{q}}$	=	vector of disturbance function variables

*Research Engineer, Computational AeroSciences Branch, NASA LaRC. AIAA Senior Member
†Research Scientist, Computational AeroSciences Branch. AIAA Fellow
‡Research Scientist, Computational AeroSciences Branch.

$\bar{\mathbf{q}}$ = vector of base flow variables
$\tilde{\mathbf{q}}$ = vector of perturbation variables
Re_∞ = freestream unit Reynolds number [m^{-1}]
Re_{R_N} = Reynolds number based on nose radius
Sch = Numerical schlieren
r_b = local radius of axisymmetric body at the axial station of interest [m]
R_N = nose radius [m]
T = temperature [K]
T_w = wall temperature [K]
$T_{w,ad}$ = adiabatic wall temperature [K]
(u, v, w) = streamwise, wall-normal, and azimuthal velocity components [$m \cdot s^{-1}$]
(x, y, z) = Cartesian coordinates
α = streamwise wavenumber [m^{-1}]
δ_h = boundary-layer thickness [m]
δ_S = entropy-layer thickness [m]
κ = streamwise curvature [m^{-1}]
ω = disturbance angular frequency [s^{-1}]
ρ = density [kg m^{-3}]
(ξ, η, ζ) = streamwise, wall-normal, and azimuthal coordinates
$\Delta\xi$ = streamwise interval considered for optimal growth analysis [m]
ΔS = entropy increment [$kg\ m^2 \cdot s^{-2} \cdot K^{-1}$]
θ = cone half-angle [°]

Superscripts

$*$ = dimensional value
H = conjugate transpose

Subscript

∞ = freestream value
T = transition location

Abbreviations

AFRL = Air Force Research Laboratory
DNS = direct numerical simulation
DPLR = data parallel-line relaxation
HLNSE = harmonic, linearized Navier-Stokes equations
MFD = mean flow distortion
NS = Navier-Stokes
LIF = laser-induced fluorescence
LPSE = linear parabolized stability equations
NPSE = nonlinear parabolized stability equations
RMS = root-mean-square

I. Introduction

Laminar-turbulent transition of boundary-layer flows can have a strong impact on the performance of hypersonic vehicles because of its influence on the surface skin friction and aerodynamic heating. Therefore, the prediction and control of transition onset and the associated variation in aerothermodynamic parameters in high-speed flows is a key issue for optimizing the performance of the next-generation aerospace vehicles. Although many practical aerospace vehicles have blunt, hemispherical and ogival nose-tips, the mechanisms that lead to boundary-layer instability and transition on such geometries are not well understood as yet. A detailed review of boundary layer transition over sharp and blunt cones in a hypersonic freestream is given by Schneider [1]. As described therein, both experimental and numerical studies have shown that the modal growth of Mack-mode instabilities (or, equivalently, the so-called second-mode waves) is responsible for laminar-turbulent transition on sharp, axisymmetric cones at zero angle of attack. Studies have also shown that increased nose-tip bluntness, i.e., radius of hemispherical or ogival nose-tips, lead to the formation of an entropy layer that can extend well beyond the vicinity of the nose-tip region [2]. This entropy layer has been shown to have a stabilizing effect on the amplification of Mack-mode instabilities, which is consistent with the

observation that the onset of transition is displaced downstream as the nose bluntness is increased. However, while the boundary layer flow continues to become more stable with increasing nose bluntness, experiments indicate that the downstream movement in transition actually slows down and eventually reverses as the nose bluntness exceeds a certain critical range of values [2]. The observed reversal in transition onset at large values of nose bluntness is contrary to the predictions from linear stability theory, and therefore, must be explained using a different paradigm. While no satisfactory explanation has been proposed as yet, one of the physical effects that is suspected to cause this transition reversal is the role of surface roughness and/or freestream turbulence. Therefore, nonmodal disturbance amplification induced by the external forcing has been recently proposed as the basis for a physics-based model of the transition reversal phenomenon [3–5].

A recent collaborative effort under the NATO STO group AVT-240 on Hypersonic Boundary-Layer Transition Prediction focused on the problem of transition on axisymmetric cones with blunt, hemispherical nose-tips and on the potential role of transient growth in the transition reversal phenomenon [3, 5]. The comparison of wind tunnel measurements at freestream Mach numbers from 6 to 12 in both U.S. and European facilities showed two distinct regions referred to as "small bluntness" where the transition location moves downstream with increased bluntness, and "large bluntness" where the transition location rapidly moves upstream. Furthermore, Stetson [2] identified an intermediate regime for "moderately-large bluntness" values, wherein transition still moves downstream as the nose bluntness is increased, but at a significantly slower rate. In these cases, the frustum transition is measured at locations where the Mack-mode waves are not sufficiently amplified and yet the transition Reynolds number is lower than that for a sharp cone at the same flow conditions. Beyond the critical nose Reynolds number for transition reversal for large bluntness values, the transition appears to depend on uncontrolled disturbances due to nose-tip roughness. The reason for the variation in the critical Reynolds numbers among the datasets is not clear as yet. The use of fast-response heat flux sensors can help to characterize the transition mechanisms on blunt cones. For instance, time-resolved heat transfer measurements performed at Mach 9 by Zanchetta [6] in the Imperial College Gun Tunnel on a 5-degree half-angle cone revealed that in the reversal regime, transitional events are formed in the near-nose region and convect downstream. The formation frequency of the events was linked to the severity of the roughness environment. The experimental investigation of roughness effect in the transition reversal regime [6] revealed that two-dimensional annular trips may be more effective to enhance transition than three-dimensional roughness. Recent laser-induced-fluorescence-based (LIF) schlieren measurements from Grossir et al. [7] on a blunt 7-degree half-angle cone at Mach 11.9 in the Von Kármán Institute Longshot hypersonic wind tunnel revealed disturbances with shapes quite different from the usual second-mode rope structures. The disturbances that extend above the edge of the boundary layer for the 4.75 mm nose-tip radius. These disturbances, that were not present on schlieren images for sharper cones, could be a manifestation of the blunt cone transition mechanism leading to the heat transfer fluctuation measured by Zanchetta [6]. However, the available linear stability analyses [8–13] agree that the frustum transition for moderately-large bluntness and transition reversal for large bluntness cannot be predicted by only considering modal instability amplification, because Mack's second mode is strongly stabilized by the presence of the entropy layer and the first mode, commonly responsible for the onset on transition at boundary-layer-edge supersonic conditions, is not destabilized. Additionally, the modal amplification of entropy-layer modes is marginal as reported by Refs. [5, 14, 15].

Because of the failure of the modal instability theory to predict the transition within the swallowing distance of the entropy layer, nonmodal growth was proposed by Paredes et al. [3] as the potential basis for a physics-based model for the experimentally observed onset of transition. Results indicate that stationary disturbances that are initiated within the nose-tip vicinity can undergo relatively significant nonmodal amplification that increases with the nose-tip bluntness. This finding does not provide a definite link between transient growth and the onset of transition, but is qualitatively consistent with the experimental observations that frustum transition during the reversal regime was highly sensitive to wall roughness, and furthermore, was dominated by disturbances originating near the nose-tip. The predictions for optimal transient growth were used to design an azimuthally periodic array of microroughness elements located near the sonic point at the nose-tip [3]. The measurements showed that variable bluntness models with similar values of roughness Reynolds number, Re_{kk}, affected transition only on the blunter cone, demonstrating that transition onset in this case is associated with the combined effects of bluntness and roughness. Furthermore, Cook et al. [4], Paredes et al. [5, 16] showed significant nonmodal growth of planar and oblique traveling disturbances that peak within the entropy layer. For moderately blunt cones, Paredes et al. [16] reported an initial nonmodal growth followed by a partial decay in disturbance amplitude that is subsequently overcome via modal growth as Mack-mode waves in the downstream region. This behavior is qualitatively consistent with the experimental observations that frustum transition in the absence of sufficient Mack-mode amplification is accompanied by a double peak in the disturbance amplification curve [10]. Furthermore, schlieren measurements based on laser-induced-fluorescence (LIF) [7] have revealed that, for a blunt,

7-degrees half-angle cone at Mach 11.9, there exist prominent disturbance structures extending above the edge of the boundary layer. It has been speculated [16] that the observed disturbances may be associated with the nonmodal amplification of traveling waves.

The present paper investigates the nonlinear evolution of the nonmodal traveling disturbances from Paredes et al. [16], which may potentially lead to laminar-turbulent transition upstream of the swallowing location of the entropy layer on a variable bluntness, 7-degree cone that was tested in the AFRL Mach-6 high-Reynolds-number facility[13]. The methodologies used to investigate the nonlinear evolution of disturbances are summarized in Section II. Then, the laminar boundary layer flow over the selected configurations and the results for planar and oblique traveling disturbances are presented in Section III. A brief summary, including the conclusions based on this study, are presented in Section IV.

II. Theory

In this section, we outline the methodologies used to study the nonlinear development of instability waves in the studied configurations. The linearly optimal perturbation that results in maximum energy gain at a specified downstream position is used as the inflow condition for the parabolic integration of the nonlinear PSE and direct numerical simulation (DNS) solvers. The inflow profiles used in the present nonlinear study are computed following the analysis of Refs. [5, 16], who used the harmonic form of the linearized Navier Stokes equations (HLNSE) and the linear parabolized stability equations (LPSE) frameworks for modal and nonmodal analysis. Details about these linear methods can be found in such references.

A. Nonlinear Parabolized Stability Equations

In what follows, we study the boundary layers over axisymmetric bodies in hypersonic freestream flows. The freestream conditions and geometries are selected to match a subset of configurations used in the experiments conducted with variable bluntness, 7-degree cones at AFRL [13]. For this problem, the computational coordinates are defined as an orthogonal body-fitted coordinate system, where (ξ, η, ζ) denote the streamwise, wall-normal, and azimuthal coordinates and (u, v, w) represent the corresponding velocity components. Density and temperature are denoted by ρ and T. The metric factors are defined as

$$h_\xi = 1 + \kappa\eta, \tag{1}$$

$$h_\zeta = r_b + \eta\cos(\theta), \tag{2}$$

where h_ξ and h_ζ are associated with the streamwise and azimuthal curvature, respectively, κ denotes the streamwise curvature, r_b is the local radius, and θ is the local half-angle along the axisymmetric surface, i.e., $\sin(\theta) = dr_b/d\xi$.

The disturbance variables are expanded in terms of their truncated Fourier components assuming they are periodic in time and can be written as

$$\tilde{\mathbf{q}}(\xi, \eta, \zeta, t) = \sum_{n=-N}^{N} \breve{\mathbf{q}}(\xi, \eta, \zeta)\exp\left[-\mathrm{i}n\omega t\right]. \tag{3}$$

The streamwise wavenumber is α and ω is the angular frequency of the perturbation. The Cartesian coordinates are represented by (x, y, z). The vector of perturbation fluid variables is $\tilde{\mathbf{q}}(\xi, \eta, \zeta, t) = (\tilde{\rho}, \tilde{u}, \tilde{v}, \tilde{w}, \tilde{T})^T$ and the vector of disturbance functions is $\breve{\mathbf{q}}(\xi, \eta) = (\breve{\rho}, \breve{u}, \breve{v}, \breve{w}, \breve{T})^T$. The vector of basic state variables is $\bar{\mathbf{q}}(\xi, \eta) = (\bar{\rho}, \bar{u}, \bar{v}, \bar{w}, \bar{T})^T$. The present study focuses on axisymmetric boundary-layer flows, and therefore, the basic state variables are homogeneous in the spanwise direction. The linear analysis conducted by Paredes et al. [16] exploited this characteristic and also introduced the Fourier decomposition of the disturbance variables in the azimuthal direction via the azimuthal wavenumber m. Here, the nonlinear, plane-marching PSE technique is used with Fourier collocation discretization along the azimuthal direction, although a nonlinear, line-marching PSE could also be used for the present flow problem.

The PSE approximation is based on isolating the rapid phase variations in the streamwise direction by introducing the ansatz

$$\breve{\mathbf{q}}(\xi, \eta, \zeta) = \hat{\mathbf{q}}(\xi, \eta, \zeta)\exp\left[\mathrm{i}\int_{\xi_0}^{\xi} \alpha(\xi')\,\mathrm{d}\xi'\right], \tag{4}$$

where the unknown wavenumber distribution $\alpha(\xi)$ is determined in the course of the solution by imposing an additional constraint

$$\int_\zeta \int_\eta \hat{\mathbf{q}}^* \frac{\partial \hat{\mathbf{q}}}{\partial \xi}\, h_\xi\, h_\zeta\, \mathrm{d}\eta\, \mathrm{d}\zeta = 0, \tag{5}$$

where the amplitude functions $\hat{\mathbf{q}}(\xi, \eta, \zeta) = (\hat{\rho}, \hat{u}, \hat{v}, \hat{w}, \hat{T})^T$ vary slowly in the streamwise direction in comparison with the phase term $\exp\left[\mathrm{i}\int_{\xi_0}^{\xi} \alpha(\xi')\,\mathrm{d}\xi'\right]$. Substituting Eq. (4) into Eq. (3) and involving the scale separation to neglect the viscous, streamwise derivative terms, one obtains the NPSE in the form

$$\left(\mathbf{L}_n + \mathbf{M}_n \frac{\partial}{\partial x}\right) \hat{\mathbf{q}}_n(x, y, z) = \mathbf{F}_n(x, y, z) \exp\left(-\mathrm{i}\int_{x_0}^{x} \alpha_n(x')\,\mathrm{d}x'\right), \tag{6}$$

where $\mathbf{F}_n$ is the Fourier component of the total forcing $\mathbf{F}$ that contains the nonlinear terms. The entries of the coefficient matrices for $\mathbf{L}_n$, $\mathbf{M}_n$ and vector $\mathbf{F}$ with a more detailed description of the method can be found in Refs. [17–19].

The discretized NPSE are integrated along the streamwise coordinate by using first-order backward differentiation. Nonuniform stable high-order finite-difference schemes [20, 21] of sixth order are used for discretization of the NPSE along the wall-normal coordinate. For the results presented here, the wall-normal direction is discretized using from $N_\eta = 201$ to $N_\eta = 401$, with the nodes being clustered toward the wall. The spanwise direction is discretized with Fourier collocation points. Depending on the amplitude of the inflow perturbation, the number of spanwise points is varied from $N_\zeta = 8$ to $N_\zeta = 32$. The number of discretization points in every direction was varied in selected cases to ensure convergence of the results.

No-slip, isothermal boundary conditions are used at the wall, i.e., $\hat{u} = \hat{v} = \hat{w} = \hat{T} = 0$. The amplitude functions are forced to decay at the farfield boundary by imposing the Dirichlet conditions $\hat{\rho} = \hat{u} = \hat{w} = \hat{T} = 0$, unless otherwise stated. The farfield boundary coordinate is set below the shock layer.

B. Direct Numerical Simulations

The three-dimensional, azimuthally-periodic, laminar boundary-layer flow over the cone surface perturbed by an inflow low-amplitude traveling wave is also computed by using a high-order DNS solver. A detailed description of the governing equations and their numerical solution is given by Wu and Martin [22]. The inviscid fluxes from the governing equations are computed using a seventh-order wighted essentially nonoscillatory finite-difference WENO scheme introduced by Jiang and Shu [23]; the present scheme also allows the use of limiters that have been optimized to reduce the numerical dissipation. Both an absolute limiter on the WENO smoothness measurement and a relative limiter on the total variation are employed simultaneously during the simulation [22]. The viscous fluxes are discretized using a fourth-order central difference scheme and time integration is performed using a third-order low-storage Runge-Kutta scheme [24].

The computational grid is based on the grid used for the NPSE calculations with 301 points in the wall-normal direction, although the number of points in the streamwise direction is increased to have a minimum of 60 points per streamwise wavelength of the fundamental wave, which resulted in a maximum of 5200 points, and the number of points in the spanwise direction was selected to allow for the solution of the initial phases of transition with a maximum of 96 points. The grid resolution was checked for convergence by comparing with the NPSE results.

III. Results

This section describes the computational predictions of the nonlinear evolution of nonmodal traveling disturbances in the boundary layer over a 7-degree blunt cone. The freestream conditions match a selected subset of conditions from the experiments by [13] in the Air Force Research Laboratory (AFRL) Mach 6 High Reynolds Number facility. In each computation, the inflow disturbance profile is obtained from the linear, optimal growth calculations presented in an earlier paper [16]. Modal instability analysis for the AFRL cone has been already performed by Jewell et al. [13]. They found that all first-mode, Mack-mode, and entropy layer disturbances were either damped or weakly unstable for the configurations of interest, and therefore, the experimentally measured transition onset cannot be predicted on the basis of modal analysis. In the absence of modal growth, the transient growth mechanism was investigated as a potential cause for the onset of transition by [3, 5, 16]. The nonmodal analysis showed that stationary three-dimensional disturbances experience the maximum energy gain. Additionally, the results showed that the nonmodal growth persists up to progressively higher disturbance frequencies when either the freestream Reynolds number or the nose-tip radius is increased, or equivalently, as the nose Reynolds number, Re_{R_N}, becomes larger. With continued increase in Re_{R_N}, one observes the emergence of a new peak in the energy gain contours within the (F, m) plane. This peak corresponds to the nonmodal amplification of planar waves ($m = 0$) that are quite distinct from the second mode instabilities.

To set the stage for the results pertaining to the nonlinear evolution of the dominant nonmodal disturbances, we begin with the basic state solutions at the conditions of interest and those are presented in subsection III.A.

A. Laminar Boundary-Layer Flow

The laminar boundary-layer flows over the blunt cones were computed by [12] with reacting, axisymmetric Navier-Stokes equations on a structured grid. The solver was a version of the NASA data parallel-line relaxation (DPLR) code [25], that is included as part of the STABL-2D software suite, as described by Johnson [26] and Johnson et al. [27]. This flow solver employs a second-order-accurate finite-volume formulation. The inviscid fluxes are based on the modified Steger-Warming flux vector splitting method with a monotonic upstream-center scheme for the conservation laws (MUSCL) limiter. The time integration method is the implicit, first-order DPLR method. The effects of chemistry and molecular vibration are negligible at the present flow conditions. Thus, the high enthalpy effects are omitted from the calculations. The viscosity law used is the Sutherland's law and the heat conductivity is calculated using Eucken's relation. Additional details about the basic state solution and the grid convergence study are given by Jewell and Kimmel [12].

The AFRL Mach 6 facility operates at stagnation pressures p_0 from 700 to 2100 psi (4.83 to 14.5 MPa). The working fluid is air and is treated as an ideal gas because of the relatively low temperature and pressure. The blunt cones used in the experiments by Stetson [2] had a half-angle of 8° and a base radius of 2.0 in. (0.0508 m). A total of 196 experiments encompassing 108 unique conditions comprised the Stetson [2] Mach 6 results. Table 1 shows the details of the configuration selected for the present analysis. The present analysis uses the 7° half-angle variable-bluntness cone that is currently used in the experiments in the AFRL Mach 6 facility by Jewell et al. [13]. The actual freestream Mach number is $M_\infty = 5.9$. The thermal wall condition is isothermal with a constant wall temperature equal to $\bar{T}_w = 300.0$ K that corresponds to a wall-to-adiabatic temperature ratio of $\bar{T}_w/\bar{T}_{w,ad} = 0.57$. The experimentally measured transition location, ξ_T, by Jewell et al. [13] are included. The predicted Mack-mode N-factor, i.e., $N_{\mathrm{MM}}(\xi_T)$, together with the corresponding disturbance frequency, $F_{\mathrm{MM}}(\xi_T)$, computed by Paredes et al. [16] are also shown in Table 1. The predicted N-factor at the measured transition location is nearly zero. Therefore, the Mack-mode instability cannot be the cause behind the transition onset observed in the experiments.

Table 1 Details of the AFRL configurations used in the present study, including the measured transition locations (ξ_T) from Ref. [13], the Mack-mode N-factor ($N_{\mathrm{MM}}(\xi_T)$) at the transition location, along with the frequency of the most amplified disturbance ($F_{\mathrm{MM}}(\xi_T)$). The flow conditions are $M_\infty = 5.9$, $\bar{T}_\infty = 76.74$ K, $\bar{T}_w = 300$ K, and $\bar{T}_w/\bar{T}_{w,ad} = 0.57$.

R_N [mm]	Re_∞ [$\times 10^6$ m^{-1}]	Re_{R_N} [$\times 10^3$]	ξ_T [m]	$N_{\mathrm{MM}}(\xi_T)$	$F_{\mathrm{MM}}(\xi_T)$ [kHz]
1.524	91.5	139.4	0.133	0.04	1340

The Mach number and entropy increment contours of the laminar boundary-layer flow from Table 1 are shown in figure 1. The streamwise domain is selected to observe the nose-tip vicinity. The entropy increment, ΔS, is defined with respect to the freestream value, i.e., $\Delta S = c_p \ln(\bar{T}/\bar{T}_\infty) - R_g \ln(\bar{p}/\bar{p}_\infty)$, where $c_p = 1004$ J $\cdot$ kg^{-1} $\cdot$ K^{-1} is the specific heat for a constant pressure and $R_g = 287.058$ J $\cdot$ kg^{-1} $\cdot$ K^{-1} is the specific gas constant. The entropy-layer edge, δ_S, is defined as the location where the local entropy increment is 0.25 times the entropy increment at the wall ($\Delta S(\xi, \eta = \delta_S) = 0.25 \Delta S_{wall}$). The entropy-layer edge approaches the boundary-layer edge as the streamwise location increases. The local Mach number remains below approximately 4.4 under the entropy-layer edge.

B. Nonlinear Evolution of Nonmodal Traveling Disturbances

The linear, nonmodal amplification characteristics at the test condition from Table 1 were computed by Paredes et al. [16]. Their results showed significant disturbance growth over a streamwise interval of $(\xi_0, \xi_1) = (0.014, 0.133)$ m preceding the measured transition location. The highest energy gain occurred for an oblique stationary disturbance with $(F, m) = (0, 68)$ and $N_E = 5.58$. The perturbations associated with this mode are mostly contained to the boundary layer region. The results from Paredes et al. [16] also show that oblique traveling disturbances experience a monotonically reduced energy amplification as the disturbance frequency is increased, and furthermore, that the traveling disturbances have a notably different structure than the stationary streaks. In particular, the peak disturbance magnitude for the oblique traveling waves is located in between the edge of the boundary layer and the outer boundary of the entropy-layer region. An additional peak in the energy amplification contours corresponds to planar traveling disturbances with a similar disturbance profile. The maximum energy gain for the planar disturbances corresponds to $F = 420$ kHz, with a logarithmic energy gain of $N_E = 3.60$. Because the traveling mode structures have a rather weak signature inside the boundary-layer region (i.e., below the edge of the boundary layer), if and how they can initiate the process of

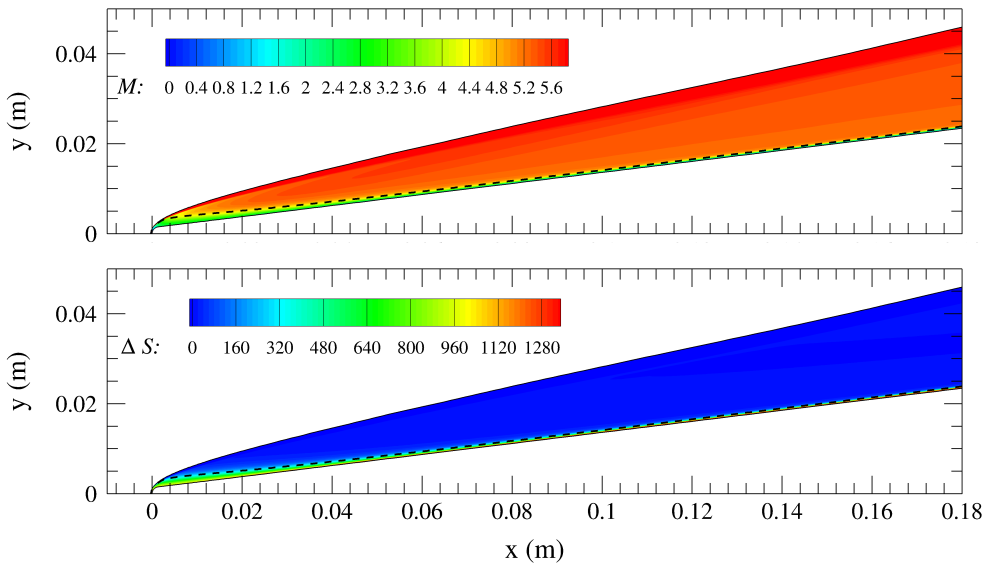

Fig. 1 Mach number (M) and entropy increment (ΔS) contours of the laminar boundary-layer flow over the AFRL configuration with $R_N = 5.08$ mm. The dashed, black line indicates the edge of the entropy layer, δ_S.

boundary-layer transition remains to be determined. To help address that question, we now investigate the possible paths to transition via nonmodal growth of traveling disturbances by studying their nonlinear evolution. The inflow disturbance for the present computations is extracted at $\xi = 0.03$ m from the linear nonmodal analysis of Paredes et al. [16] for a streamwise interval of $(\xi_0, \xi_1) = (0.014, 0.133)$ m. First, an inflow disturbance composed of a pair of oblique traveling waves with $F = 250$ kHz and $m = \pm 50$ is used to investigate the possibility of an oblique-mode breakdown. Second, the nonlinear development of a planar wave with $F = 500$ kHz is studied as a potential precursor to transition via a fundamental- or subharmonic-type secondary instability.

1. Oblique traveling waves

First, an inflow disturbance composed of a pair of oblique traveling waves with $F = 250$ kHz and $m = \pm 50$ is introduced into the NPSE and DNS computations. Computations are performed for two different inflow amplitudes. The lower amplitude case corresponds to $|\tilde{u}_1|_{max}/u_\infty = 7.13 \times 10^{-6}$, aimed at cross-validating the PSE and DNS predictions for the case of a nearly linear evolution. The higher amplitude case is aimed at investigating nonlinear effects on the nonmodal growth, and corresponds to an initial amplitude that is 100 times larger, i.e., $|\tilde{u}_1|_{max}/u_\infty = 7.13 \times 10^{-4}$.

Figure 2 shows the streamwise evolution of the root-mean-square (RMS) of the streamwise velocity disturbance corresponding to the fundamental frequency, the mean-flow-distortion (MFD), and the harmonics created via nonlinear effects. The low amplitude, quasilinear case from figure 2(a) indicates an excellent agreement between the linear prediction based on LPSE and the nonlinear predictions obtained with NPSE and DNS. The higher amplitude case of figure 2(b) also shows a good agreement between the three methodologies, but the nonlinear predictions begin to deviate from the linear curve around $\xi = 0.1$ m. From this location, the nonlinear effects become appreciable, but the NPSE and DNS continue to agree, with the exception of minor discrepancies for the higher harmonics. However, as the disturbance amplitude becomes sufficiently large, the NPSE marching fails to converge, starting at approximately $\xi = 0.135$ m. For both initial amplitudes, the MFD experiences a rapid growth starting from $\xi \approx 0.07$ m. This abrupt change in the slope of the MFD amplitude curve is caused by a switchover in the peak location of the MFD profile, from an outer peak in the entropy layer upstream of $\xi \approx 0.07$ m to an inner peak within the boundary-layer region for $\xi > 0.07$ m. The considerably faster growth in the MFD magnitude along the inner peak is clearly evidenced from the change in the slope of the MFD amplitude curve. Figure 3 shows a three-dimensional view of the isosurfaces of streamwise velocity disturbance for the MFD, fundamental, and first harmonic modes for the case of the high initial amplitude from figure 2(b). The fundamental mode also peaks within the entropy layer at a sufficiently upstream location, i.e., significantly farther out from the boundary layer edge, but the peak location approaches the boundary layer edge with an increasing downstream distance. The emergence of the stationary streaks associated with the MFD mode coincides with

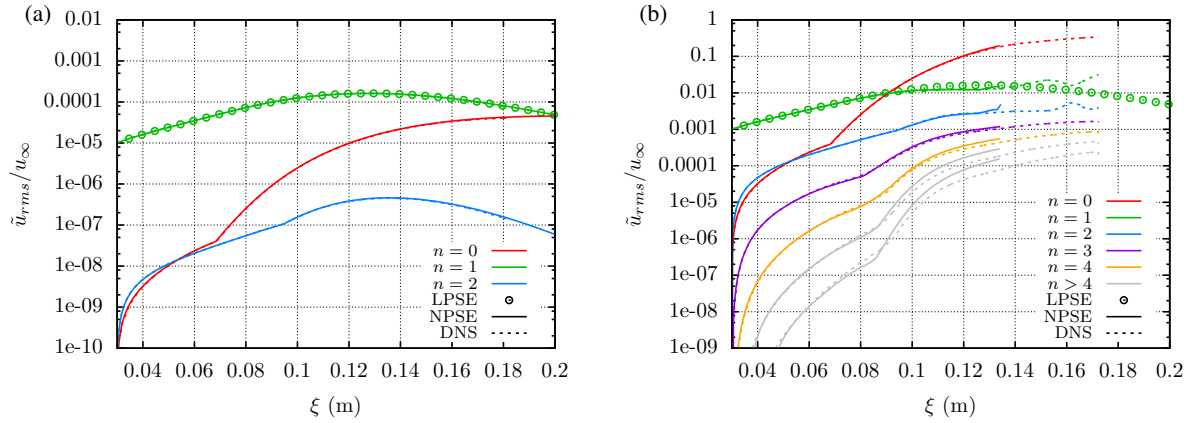

Fig. 2 Root-mean-square evolution of streamwise velocity disturbance computed with NPSE and DNS for a fundamental disturbance composed by a pair of traveling waves with $F = 250$ kHz and $m = \pm 50$ with an initial amplitude of (a) $|\tilde{u}_1|_{max}/u_\infty = 7.13 \times 10^{-6}$ and (b) $|\tilde{u}_1|_{max}/u_\infty = 7.13 \times 10^{-4}$. The linear evolution of the fundamental mode computed with LPSE is also included.

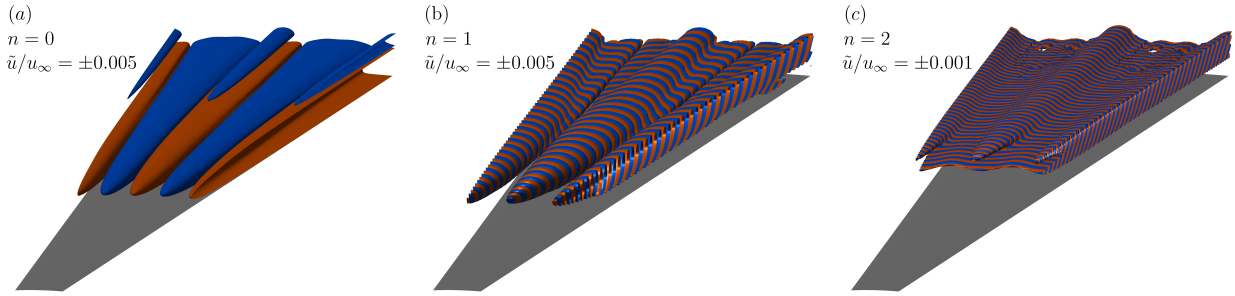

Fig. 3 Positive (red) and negative (blue) isosurfaces of streamwise velocity disturbance of (a) MFD, (b) fundamental, and (c) first harmonic modes computed with DNS for an initial disturbance composed by a pair of traveling waves with $F = 250$ kHz and $m = \pm 50$ with an initial amplitude of $|\tilde{u}_1|_{max}/u_\infty = 7.13 \times 10^{-4}$.

the axial location where the peak fundamental fluctuations approach the edge of the mean boundary layer from above. The stationary streaks continue to amplify downstream, resulting in a strong azimuthal modulation of the boundary layer flow. Disturbances at the first harmonic ($F = 500$ kHz) of the fundamental disturbance are initially dominated by the axisymmetric wave created by the nonlinear interaction between the pair of oblique waves at the fundamental frequency of $F = 250$ kHz. Farther downstream, however, the disturbance motion at all three leading frequencies (i.e., MFD, fundamental, and the first harmonic) develop a more complex structure, involving an azimuthal modulation of the initial axisymmetric disturbance at $F = 500$ kHz by the stationary streaks as well as the appearance of higher harmonics in the azimuthal direction.

Figure 4 shows the isolines of the stationary streamwise velocity corresponding to the superposition of the unperturbed, laminar basic state and the MFD mode, together with the isocontours of the fundamental mode. Both sets of contours clearly highlight the azimuthal modulation of the boundary layer due to the finite amplitude streaks at twice the azimuthal wavenumber of the primary, traveling mode disturbance. Furthermore, the streaks become unstable and the disturbance at the fundamental frequency transitions to a sinuous instability corresponding to a subharmonic of the streak spacing. This sinuous disturbance increases in amplitude (albeit in a non-monotonic fashion due to what appears to be a cyclic exchange in energy with the first harmonic at $F = 500$ kHz) and may eventually lead to a breakdown of the streaks.

Figure 5 shows the evolution of the skin friction coefficient for both the laminar basic state and for the case of higher initial amplitude from figure 2(b). The NPSE and DNS skin friction predictions agree until the PSE marching fails to converge and they both show a deviation from the laminar curve for $\xi > 0.11$ m, with a minimum in the skin friction

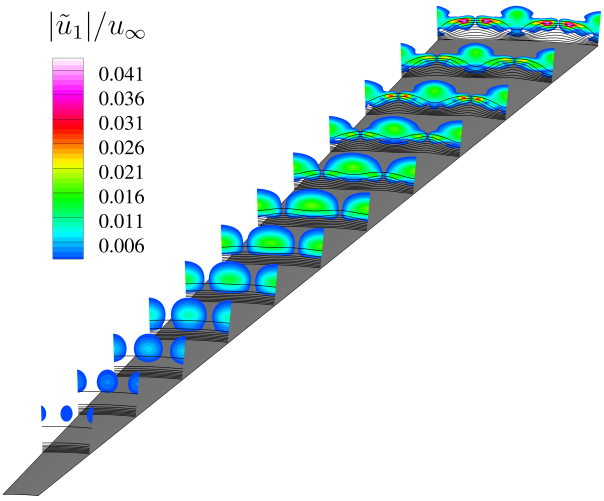

Fig. 4 Streamwise velocity magnitude isocontours of the fundamental mode and streamwise velocity isolines of the superposition of the basic flow and the MFD computed with DNS for an initial disturbance composed by a pair of traveling waves with $F = 250$ kHz and $m = \pm 50$ with an initial amplitude of $|\tilde{u}_1|_{max}/u_\infty = 7.13 \times 10^{-4}$.

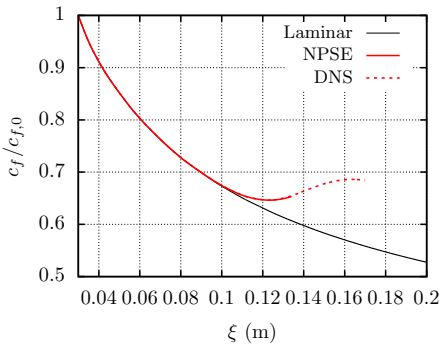

Fig. 5 Evolution of the normalized skin friction coefficient for the nonlinear evolution of an initial disturbance composed by a pair of traveling waves with $F = 250$ kHz and $m = \pm 50$ with an initial amplitude of $|\tilde{u}_1|_{max}/u_\infty = 7.13 \times 10^{-4}$ computed with NPSE and DNS. The laminar values are included as a reference.

coefficient at $\xi = 0.123$ m. Although not shown here, equivalent results are found for the heat transfer coefficient, with the minimum at a slightly downstream location of $\xi = 0.127$ m. The NPSE method is able to reach the initial rise of skin friction and heat transfer coefficients, in close agreement with the DNS prediction. Therefore, NPSE provides an efficient technique for the parametric study of the initial phase of the nonlinear development of this type of nonmodal traveling disturbances up to and somewhat beyond the initial rise in skin friction. Heat transfer measurements during the experiments at AFRL Ref. [13] showed that the heat transfer coefficient first increased above the laminar value near $\xi = 0.133$ m. The present results indicate that a noticeable increase in skin friction and heat transfer can occur at a similar location as a result of the nonlinear interactions initiated by a pair of nonmodal traveling waves, even in the absence of any modal growth associated with the Mack mode of instability.

The rise in skin friction from figure 5 may or may not signify the onset of transition and could be associated simply with the finite amplitude stationary streaks within the boundary layer region. The relationship, if any, between the initial rise in skin friction and an impending onset of transition can be established only via additional DNS computations extending over a larger domain and/or for higher inflow amplitudes. Nonetheless, the NPSE and DNS computations described in this section have provided a viable mechanism through which the entropy layer disturbances can penetrate the boundary layer region and pave the way for a potential onset of transition via an enhanced growth of fluctuations in the azimuthally modulated flow.

2. Planar traveling waves

Next, we consider the case of an axisymmetric inflow disturbance with $F = 500$ kHz. In this case, three-dimensional disturbances are not considered. Following the previous analysis, the inflow disturbance is extracted at $\xi = 0.03$ m from the linear nonmodal analysis of Paredes et al. [16] with $(\xi_0, \xi_1) = (0.014, 0.133)$ m. The initial amplitude is set to $|\tilde{u}_1|_{max}/u_\infty = 8.4 \times 10^{-4}$ and 3.3×10^{-3}.

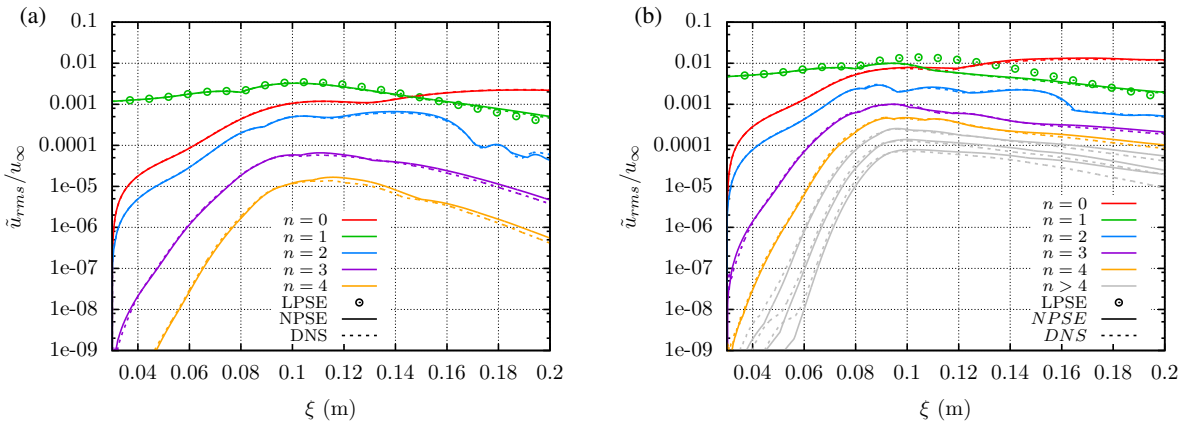

Fig. 6 Root-mean-square evolution of streamwise velocity disturbance component computed with NPSE and DNS for a fundamental disturbance with $F = 500$ kHz, $m = 0$ and an initial amplitude of (a) $|\tilde{u}_1|_{max}/u_\infty = 8.4 \times 10^{-4}$ and (b) $|\tilde{u}_1|_{max}/u_\infty = 3.3 \times 10^{-3}$. The linear evolution of the fundamental mode computed with LPSE is included.

Figure 6 shows the streamwise evolution of the RMS of the streamwise velocity disturbance for the MFD ($n = 0$), the fundamental frequency ($n = 1$), and its higher harmonics ($n > 1$). The agreement between the NPSE and DNS predictions is excellent. Nonlinear effects at both initial amplitudes are evident from the deviation of the fundamental mode evolution from the linear prediction obtained via LPSE; specifically, figure 6(a) shows a deviation in the fundamental mode amplitude starting from $\xi \approx 0.1$ m for the lower initial amplitude case, while figure 6(b) shows a different evolution between the nonlinear and linear predictions from $\xi \approx 0.08$ m onward. In both cases, the maximum amplitude based on the nonlinear computations is lower than that from the linear prediction, indicating an initially stabilizing influence of nonlinear effects on the fundamental mode evolution. Also, the nonlinearity becomes sufficiently strong in both cases so that the amplitude of the MFD overcomes that of the fundamental wave.

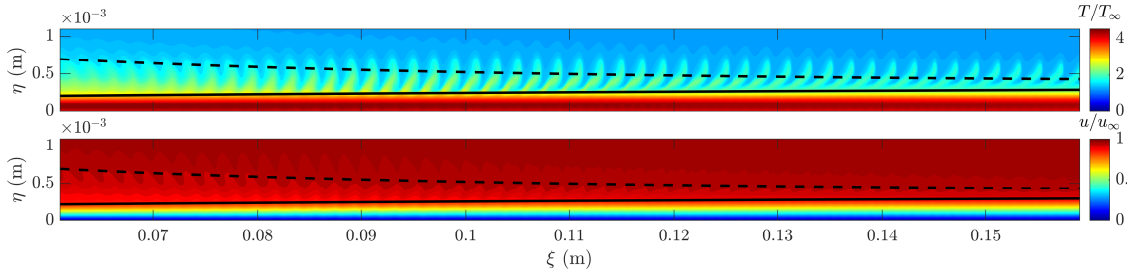

Fig. 7 Contours of temperature and streamwise velocity components of the total flow computed with DNS for a fundamental disturbance with $F = 500$ kHz, $m = 0$ and an initial amplitude of $|\tilde{u}_1|_{max}/u_\infty = 3.3 \times 10^{-3}$. The solid and dashed black lines indicate the edges of the boundary layer, δ_h, and the entropy layer, δ_S, respectively.

The temperature and streamwise velocity components of the perturbed boundary-layer flow, which is composed of the basic flow and the total perturbation field, for the planar inflow disturbance with $|\tilde{u}_1|_{max}/u_\infty = 3.3 \times 10^{-3}$ is shown in figure 7. The appearance of inclined structures above the boundary-layer edge is evident from the temperature contours, although these structures are hardly distinguishable in the streamwise velocity figure. These inclined structures are strongly reminiscent of the transitional events observed during blunt cone experiments by using schlieren flow visualizations [7, 28]. To allow for a qualitative comparison with the experimental schlieren images, figure 8 shows the

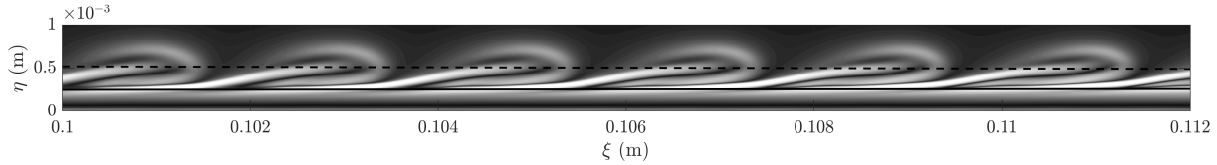

Fig. 8 Contours of numerical schlieren of the total flow computed with DNS for a fundamental disturbance with $F = 500$ kHz and $m = 0$ with an initial amplitude of $|\tilde{u}_1|_{max}/u_\infty = 3.3 \times 10^{-3}$. The same scale is applied in both axis. The solid and dashed black lines indicate the edges of the boundary layer, δ_h, and the entropy layer, δ_S, respectively.

isocontours from the numerical schlieren that was defined after Ref. [22] as

$$Sch(\xi, \eta) = c_1 \exp\left[-c_2((|\nabla\rho| - |\nabla\rho|_{min})/(|\nabla\rho|_{max} - |\nabla\rho|_{min}))\right], \tag{7}$$

where the constants are set to $c_1 = 1.0$ and $c_2 = 5.0$, and

$$|\nabla\rho| = \sqrt{\left(\frac{1}{h_\xi}\frac{\partial\rho}{\partial\xi}\right)^2 + \left(\frac{\partial\rho}{\partial\eta}\right)^2}. \tag{8}$$

A possible route to transition onset via nonlinear saturation of these planar waves would involve three-dimensional secondary instability as demonstrated for planar waves in incompressible and compressible boundary layers [29–31] or planar Mack-mode waves in hypersonic boundary layers [32].

IV. Summary and Concluding Remarks

The present paper represents an extension of the studies of Paredes et al. [5, 16], who investigated the linear, nonmodal optimal growth of stationary and traveling disturbances over a 7° half-angle, variable-bluntness cone at zero degrees angle of attack, with bluntness and freestream conditions corresponding to a subset of the experiments by Stetson [2] and Jewell et al. [13] in the AFRL Mach 6 High Reynolds Number facility. The nonmodal growth analyses from Refs. [5, 16] showed a significant energy gain upstream of the measured transition location for both stationary streaks and planar and oblique traveling disturbances initiated near the nose tip. Transition mechanisms for stationary streaks in high-speed boundary layers have been described in previous works. However, because the peak fluctuations associated with the nonmodal traveling disturbances occur outside the boundary layer region, their role in initiating boundary-layer transition was unclear. The present study has used nonlinear parabolized stability equations (NPSE) and direct numerical simulations (DNS) to investigate the potential transition mechanisms involving nonmodal traveling disturbances for the blunt cone configurations with $R_N = 1.524$ mm and $Re_\infty = 91.4 \times 10^6$ m^{-1}, for which the modal growth of Mack-mode waves at the measured transition location is known to be negligible, i.e., $N_{\mathrm{MM}} = 0.04$.

Results are presented for two classes of inflow disturbances, namely, a pair of oblique traveling waves with equal but opposite azimuthal wavenumbers of $m = \pm 50$ and a disturbance frequency of $F = 250$ kHz, and an axisymmetric traveling wave with a disturbance frequency of $F = 500$ kHz. For both classes of inflow disturbances, NPSE and DNS predictions were found to be in excellent agreement, demonstrating that the NPSE is an accurate and efficient technique for predicting the initial phase of nonlinear development of the above nonmodal traveling disturbances, including the initial rise in skin friction and heat transfer in the case of the 3D inflow disturbance. Results for the pair of oblique traveling waves show that for a modest initial amplitude of $|\tilde{u}|_{max}/u_\infty = 7.13 \times 10^{-4}$, the nonlinear interactions lead to the generation of stationary streaks inside the boundary layer that facilitate the amplification of a subharmonic sinuous disturbance and can lead to a noticeable increase in skin friction and heat transfer near the experimentally measured location of increase in surface heat flux. Furthermore, the nonlinear development of the planar traveling waves with initial amplitudes of the order of $|\tilde{u}|_{max}/u_\infty = O(10^{-3})$ lead to the formation of inclined structures that are visible in both temperature contours and numerical schlieren images. These structures are located just above the boundary-layer edge and are strongly reminiscent of the transitional events observed in the schlieren flow visualizations during hypersonic experiments with blunt cones at zero degrees angle of attack.

We note that while the present results may provide a potential explanation for transition in blunt cones upstream of the entropy swallowing location when the modal growth of Mack-mode disturbances is too weak, the origin of these

nonmodal traveling disturbances that peak within the entropy layer was not addressed; this question will be targeted in a follow-on study. Accompanying work has also investigated the effect of controlled surface roughness array in the nose tip region and the role of wake disturbances. The results of that study will be reported in a separate paper.

Acknowledgments

This research was sponsored by the NASA Transformational Tools and Technologies (TTT) Project of the Transformative Aeronautics Concepts Program (TACP) and by the Hypersonic Technology Project (HTP) under the Aeronautics Research Mission Directorate (ARMD). A portion of the computational resources supporting this work were provided by the NASA High-End Computing (HEC) Program through the NASA Advanced Supercomputing (NAS) Division at Ames Research Center. The authors would like to thank Drs. Jewell, Kimmel, Marineau, Laurance, and Schneider, and Mr. Kennedy for various technical discussions related to this topic. Additionally, we are grateful to Dr. Jewell for making the basic state computations from Ref. [13] available for this study.

References

[1] Schneider, S., "Hypersonic Laminar-Turbulent Transition on Circular Cones and Scramjet Forebodies," *Progress in Aerospace Sciences*, Vol. 40, 2004, pp. 1–50. doi:10.1016/j.paerosci.2003.11.001.

[2] Stetson, K., "Nosetip Bluntness Effects on Cone Frustum Boundary Layer Transition in Hypersonic Flow," AIAA Paper 83-1763, 1983. doi:10.2514/6.1983-1763.

[3] Paredes, P., Choudhari, M., Li, F., Jewell, J., Kimmel, R., Marineau, E., and Grossir, G., "Nosetip Bluntness Effects on Transition at Hypersonic Speeds: Experimental and Numerical Analysis Under NATO STO AVT-240," AIAA Paper 2018-0057, 2018. doi:10.2514/6.2018-0057.

[4] Cook, D., Thome, J., Brock, J., Nichols, J., and Candler, G., "Understanding Effects of Nose-Cone Bluntness on Hypersonic Boundary Layer Transition using Input-Output Analysis," AIAA Paper 2018-0378, 2018. doi:10.2514/6.2018-0378.

[5] Paredes, P., Choudhari, M., Li, F., Jewell, J., Kimmel, R., Marineau, E., and Grossir, G., "Nosetip Bluntness Effects on Transition at Hypersonic Speeds: Experimental and Numerical Analysis," *Journal of Spacecraft Rockets*, Vol. 56, No. 2, 2019. doi:10.2514/1.A34277.

[6] Zanchetta, M., "Kinetic Heating and Transition Studies and Hypersonic Speeds," Ph.D. thesis, Imperial College of Science, Technology and Medicine, London, 1996. URL `https://spiral.imperial.ac.uk/handle/10044/1/37124`.

[7] Grossir, G., Pinna, F., Bonucci, G., Regert, T., Rambaut, P., and Chazot, O., "Hypersonic Boundary Layer Transition on a 7 Degree Half-Angle Cone at Mach 10," AIAA Paper 2014-2774, 2014. doi:10.2514/6.2014-2779.

[8] Malik, M., Spall, R., and Chang, C.-L., "Effect of Nose Bluntness on Boundary Layer Stability and Transition," AIAA Paper 90-0112, 1990. doi:10.2514/6.1990-112.

[9] Herbert, T., and Esfahanian, V., "Stability of Hypersonic Flow over a Blunt Body," AGARD CP-514. Paper 28. Theoretical and Experimental Methods in Hypersonic Flows, 1994.

[10] Marineau, E., Moraru, C., Lewis, D., Norris, J., Lafferty, J., Wagnild, R., and Smith, J., "Mach 10 Boundary-Layer Transition Experiments on Sharp and Blunted Cones," AIAA Paper 2014-3108, 2014. doi:10.2514/6.2014-3108.

[11] Marineau, E., "Prediction Methodology for Second-Mode-Dominated Boundary-Layer Transition in Hypersonic Wind Tunnels," *AIAA Journal*, Vol. 55, No. 2, 2017, pp. 484–499. doi:10.2514/1.J055061.

[12] Jewell, J., and Kimmel, R., "Boundary Layer Stability Analysis for Stetson's Mach 6 Blunt Cone Experiments," *Journal of Spacecraft Rockets*, Vol. 54, No. 1, 2017, pp. 258–265. doi:10.2514/1.A33619.

[13] Jewell, J., Kennedy, R., Laurence, S., and Kimmel, R., "Transition on a Variable Bluntness 7-Degree Cone at High Reynolds Number," AIAA Paper 2018-1822, 2018. doi:10.2514/6.2018-1822.

[14] Dietz, G., and Hein, S., "Entropy-Layer Instabilities over a Blunted Flat Plate in Supersonic Flow," *Physics of Fluids*, Vol. 11, No. 1, 1999, pp. 7–9. doi:10.1063/1.869899.

[15] Fedorov, A., and Tumin, A., "Evolution of Disturbances in Entropy Layer on Blunted Plate in Supersonic Flow," *AIAA Journal*, Vol. 42, No. 1, 2004, pp. 89–94. doi:10.2514/1.9033.

[16] Paredes, P., Choudhari, M., Li, F., Jewell, J., and Kimmel, R., "Nonmodal Growth of Traveling Waves on Blunt Cones at Hypersonic Speeds," AIAA Paper 2019-0876, 2019. doi:10.2514/6.2019-0876.

[17] Paredes, P., Choudhari, M., and Li, F., "Instaiblity Wave-Streak Interactions in a Supersonic Boundary Layer," *Journal of Fluid Mechanics*, Vol. 831, 2017, pp. 524–553. doi:10.1017/jfm.2017.630.

[18] Paredes, P., Hanifi, A., Theofilis, V., and Henningson, D., "The Nonlinear PSE-3D Concept for Transition Prediction in Flows With a Single Slowly-Varying Spatial Direction," *Procedia IUTAM*, Vol. 14C, 2015, pp. 35–44.

[19] Paredes, P., "Advances in Global Instability Computations: from Incompressible to Hypersonic Flow," Ph.D. thesis, Universidad Politécnica de Madrid, 2014.

[20] Hermanns, M., and Hernández, J., "Stable High-Order Finite-Difference Methods Based on Non-Uniform Grid Point Distributions," *International Journal for Numerical Methods in Fluids*, Vol. 56, 2008, pp. 233–255. doi:10.1002/fld.1510.

[21] Paredes, P., Hermanns, M., Le Clainche, S., and Theofilis, V., "Order 10^4 Speedup in Global Linear Instability Analysis using Matrix Formation," *Computer Methods in Applied Mechanics and Engineering*, Vol. 253, 2013, pp. 287–304. doi: 10.1016/j.cma.2012.09.014.

[22] Wu, M., and Martin, M., "Direct Numerical Simulation of Supersonic Boundary Layer over a Compression Ramp," *AIAA Journal*, Vol. 45, No. 4, 2007, pp. 879–889. doi:10.2514/1.27021.

[23] Jiang, G., and Shu, C., "Efficient Implementation of Weighted ENO Schemes," *Journal of Computational Physics*, Vol. 126, No. 1, 1996, pp. 202–228. doi:10.1006/jcph.1996.0130.

[24] Williamson, J., "Low-Storage Runge-Kutta Schemes," *Journal of Computational Physics*, Vol. 35, No. 1, 1980, pp. 48–56. doi:10.1016/0021-9991(80)90033-9.

[25] Wright, M., Candler, G., and Bose, D., "Data-Parallel Line Relaxation Method for the Navier-Stokes Equations," *AIAA Journal*, Vol. 36, No. 9, 1998, pp. 1603–1609. doi:10.2514/2.586.

[26] Johnson, H., "Thermochemical Interactions in Hypersonic Boundary Layer Stability," Ph.D. thesis, University of Minnesota, 2000.

[27] Johnson, H., Seipp, T., and Candler, G., "Numerical Study of Hypersonic Reactig Boundary Layer Transition on Cones," *Physics of Fluids*, Vol. 10, No. 10, 1998, pp. 2676–2685. doi:10.1063/1.869781.

[28] Kennedy, R., Jagde, E., Laurance, S., Jewell, J., and Kimmel, R., "Visualizations of Hypersonic Boundary-Layer Transition on a Variable Bluntness Cone," AIAA Paper 2019-XXXX (accepted), 2019. doi:10.2514/6.2019-XXXX.

[29] Herbert, T., "Secondary Instability of Boundary Layers," *Annunal Review of Fluid Mechanics*, Vol. 20, 1988, pp. 487–526. doi:10.1146/annurev.fl.20.010188.002415.

[30] El-Hady, N., "Spatial Three-Dimensional Secondary Instability of Compressible Boundary-Layer," *AIAA Journal*, Vol. 29, No. 5, 1991, pp. 688–696. doi:10.2514/3.10642.

[31] Ng, L., and Erlebacher, G., "Secondary Instabilities in Compressible Boundary Layers," *Physics of Fluids*, Vol. 4, No. 4, 1992, pp. 710–726. doi:10.1063/1.858290.

[32] Li, F., Choudhari, M., Chang, C.-L., and White, J., "Secondary Instability of Second Mode Disturbances in Hypersonic Boundary Layers," PAPER NBR - 13, Proceedings of RTO-MP-AVT-200 Specialists Meeting on Hypersonic Boundary Layer Transition, San Diego, CA, April 16-19, 2012, 2012.